

Monitoring of water content in a porous reservoir by seismic data: A 3D simulation study

M. Khalili^a, P. Göransson^c, J.S. Hesthaven^b,
A. Pasanen^d, M. Vauhkonen^a, and T. Lähivaara^a

^aDepartment of Applied Physics, University of Eastern Finland, Kuopio, Finland

^bComputational Mathematics and Simulation Science,

Ecole Polytechnique Fédérale de Lausanne, Lausanne, Switzerland

^cDepartment of Aeronautical and Vehicle Engineering,

KTH Royal Institute of Technology, Stockholm, Sweden

^dGeological Survey of Finland, Kuopio, Finland

November 28, 2022

Abstract

A potential framework to estimate the amount of stored water in a porous storage reservoir from seismic data is neural networks. In this work, the water storage reservoir system is modeled as a coupled poroviscoelastic-viscoelastic medium and the underlying wave propagation problem is solved using a three-dimensional (3D) discontinuous Galerkin method coupled with an Adams-Bashforth time stepping scheme. The wave problem solver is used to generate databases for the neural network model to estimate the water content in almost real-time. In the numerical examples, we investigate a deconvolution-based approach to normalize the effect from the source wavelet in addition to the network's tolerance for noise levels. We also apply a SHapley Additive exPlanations (SHAP) analysis to get more insight into which part of the input data is contributing most to the water content estimation. The numerical results demonstrate the capacity of the fully connected neural network for estimating the amount of stored water in the porous storage reservoir.

1 Introduction

Groundwater is one of the primary water sources for agriculture and domestic usage. However, the mismanagement and unsustainable use of the existing water resources create diverse problems such as water-level drawdown and drought. Therefore, the management of groundwater resources is a key component of sustainable future development [2].

Characterization of the groundwater storage has always been challenging by conventional methods such as boreholes, coring, and trial pits, see for example [31]. These approaches are typically time consuming, expensive, and provide only spot data, see for example [7, 4]. To remedy these challenges, a direct characterization using seismic data maybe an approach for acquiring the hydrological parameters of the subsurface. As the seismic waves propagate in the ground, they capture information about the ground properties. This information includes, for example, the reflections from the discontinuities and attenuation caused by the media.

As a result, numerous geophysical studies have been devoted to predicting groundwater levels and groundwater storage. For example, a case study [25] used a combination of geophysical techniques, namely ground-penetrating radar, seismic refraction, and time-lapse gravity surveying, for estimating the groundwater storage on a field site in the Canadian Rockies. In [11], temporal and spatial variations in groundwater levels are predicted in San Gabriel Valley, California, using perturbations in seismic velocity caused by ambient seismic noise. As a third example, we refer to [24], in which seismic interferometry techniques were used to infer the space-time evolution of relative changes in seismic velocity as a measure of hydrological parameters, including groundwater fluctuations. In this last example, the groundwater basins near Los Angeles, California, were used as test areas.

In general, the groundwater exploration can be categorized into two types. One is to search for new resources while the other is the monitoring of existing water reservoirs. In this paper, the main focus is on a methodology applicable for monitoring purposes. More specifically, the objective is to estimate the water content in a man-made sand pool using seismic full waveform data. The sand pool represents an unconfined water storage reservoir underlain by impermeable clay lining. The source and receivers are placed on the ground surface for the studied three-dimensional benchmark problem. The water storage reservoir consists of two zones, namely the air-saturated and water-saturated. As a physical model for wave propagation in the saturated porous medium, we use isotropic Biot's poroviscoelastic model, while in a narrow zone next to the porous material we use the isotropic viscoelastic solid model. The water table is expected to be sharp, with no partially saturated zone, and it is allowed to fluctuate freely.

The approach studied in this work consists of two main components, namely the forward and the inverse problems.

- The first component models wave propagation from source to receiver. In this paper, wave propagation is modeled by the nodal discontinuous Galerkin (DG) method [17]. The DG method is a well-suited approach to accurately simulate wave propagation. The DG method can be used to accurately model material discontinuities, handles complex geometries, and enables efficient computations both in the central processing unit (CPU) and graphics processing unit (GPU) computational environments. The DG method has been studied in the context of wave problems by many

authors, see for example [12], [34], [37], [32], [35], [13].

- The inverse problem is solved using neural networks, which provide an efficient framework to analyze seismic data and has been studied by several authors. These studies include convolutional neural networks (CNN) for earthquake detection and location from seismograms [30]. Another example is a synthetic two-dimensional study [20], in which CNNs were used to recover the water table level and amount of stored water in an aquifer. Finally, in [6] CNNs were used to estimate subsurface velocity profiles. For a recent review of the neural networks on seismic data, we refer to [28].

In this work, the use of neural networks is motivated by the fact that they can be trained to recover the amount of stored water from synthetic seismic data. On the other hand, once the time-demanding training phase is done, the estimates can be obtained in real-time even with a standard office computer. Model interpretability is important for understanding how different data components contribute to the estimates. For this purpose, we apply the SHapley Additive exPlanations (SHAP) framework [23] to investigate the data contribution at the receiver level. Note that our intention with the SHAP analysis was to investigate the contribution of different receivers rather than developing optimal receiver array configurations.

One of the common source types in seismic surveys is to hit a metal plate that is placed on the ground surface by a sledgehammer. This leads to an unknown source wavelet that in turn would be needed to be captured in the full waveform inversion. In principle, it is possible to record, for example, the vibrations of the steel plate but these may contain data from multiple reflections and hence cannot be considered as a pure source wavelet anymore. On the other hand, it is possible to consider the source wavelet as an additional unknown parameter (or parameters) that can be estimated during the inversion procedure. In this paper, we utilize the source-independent inversion using the deconvolution of the observed wavefield with a reference trace in the frequency domain, [21, 16]. In this way, the effect of the shape of the source function can be eliminated from the traces.

2 Problem description

As the benchmark problem geometry, we study a small scale sand pool with known dimensions. In addition, we assume that the material is isotropic and homogeneous. Specifically, the geometry consists of a porous material and the surrounding elastic material, see Fig. 1. Furthermore, the porous material is divided into air-saturated and water-saturated subdomains by a water table. The geometry of the model is a box with a length 31.5 m, width 16.2 m, and height 2.75 m. In addition, the corners of the geometry are rounded as shown in the graph. The maximum length and width of the water-saturated zone are 29.5 m and 14.2 m, respectively. Finally, the bottom profile of the air-saturated zone is a rectangle with a length 23.5 m and a width 8.2 m. The clay-lined bottom is located at a depth 2 m from the top surface.

Figure 1 shows the problem geometry with a water table level at $z = -1$ m. We assume a free boundary condition on the top surface while other boundaries are modeled

as absorbing boundaries. In addition, we assume a total of 34 receivers to capture the solid velocity components v_s and w_s , i.e. the time derivatives of the corresponding solid displacements. 33 of these receivers are divided into three lines, leading to 11 sensors on each line. Receiver lines are placed parallel to the y -axis. For each line, the y coordinates are distributed uniformly over the range $y \in [-5, 5]$ m while the x -coordinate is 0.5 m for line 1, -2 m for line 2, and 3 m for line 3. One extra receiver, illustrated by a green dot symbol, is located at $(x, y) = (1, -2)$ m and is used as a reference point. A more detailed discussion of the reference point will be given later in Section 2.2. The source location is set to $(x, y) = (0.5, -1.5)$ m. Receivers and the source are placed on the ground surface ($z = 0$ m).

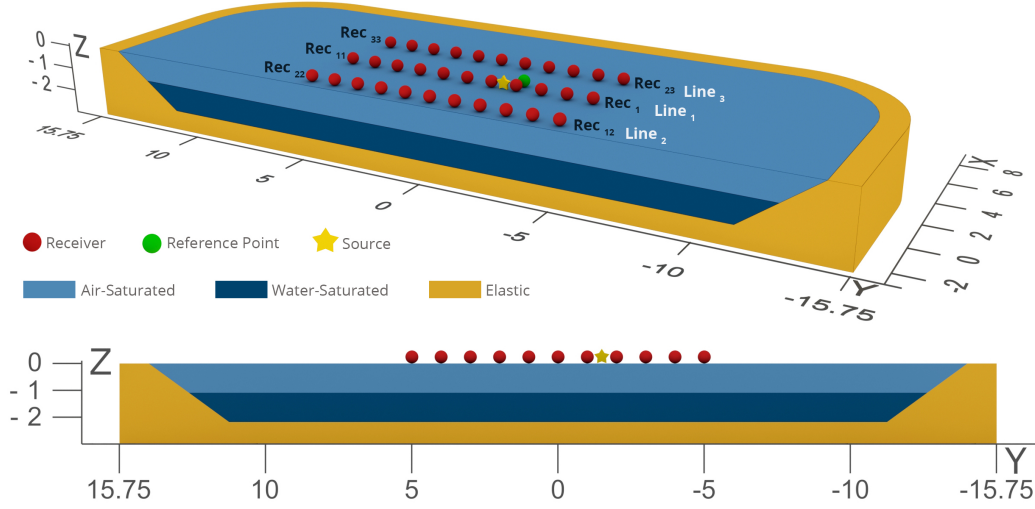


Figure 1: A cross section of the problem geometry. Light-blue color refers to air-saturated and dark-blue to water-saturated zone. Light-brown color denotes the surrounding elastic material. The setup contains a total of 34 receivers, marked with red dots and one green dot, all of which are located on the ground surface. The source location is marked with a yellow star and placed between receivers 4 and 5.

In this work, the seismic source is modeled as a point (impulse) source of force-type. The force is directed along the negative z -axis. In this study, we use two types of source wavelets. Namely a Gaussian

$$g = -\exp(a(t - t_0)^2), \quad (1)$$

where $a = -(500\pi)^2$ and a first derivative of a Gaussian

$$g = \frac{(t - t_0)}{c} \exp(b((t - t_0)^2 - c^2)), \quad (2)$$

where $b = -(f\pi)^2$ and $c = \sqrt{-0.5/b}$. The constant c is used to normalize the source function amplitude to $[-1, 1]$. In the following simulations, we set frequency f to 60 Hz, time delay t_0 to $1.2/f$, and modelling time to 0.2 s.

2.1 Physical parameters

The fluid parameters for the water-saturated subdomain are given by: the density $\rho_f = 1000 \text{ kg/m}^3$, the fluid bulk modulus $\kappa_f = 2.1025 \text{ GPa}$, and the viscosity $\eta = 1.14\text{e-}3 \text{ Pa}\cdot\text{s}$, while in the air-saturated part, we set: $\rho_f = 1.2 \text{ kg/m}^3$, $\kappa_f = 1.3628\text{e}5 \text{ Pa}$, and $\eta = 1.8\text{e-}5 \text{ Pa}\cdot\text{s}$. The quality factor Q_{κ_f} is set to a large value. All other material parameters of the water storage reservoir are assumed to be randomized from uniform distributions. Minimum and maximum values are given in Table 1. Permeability is approximated from the Kozeny-Carman equation [8]

$$k = \frac{D_p^2 \phi^3}{180(1 - \phi)^2}, \quad (3)$$

where the mean grain size D_p of the sand is set to 0.0001 m . Finally, in the surrounding viscoelastic material, we assume: $\lambda_e = 4.025 \text{ GPa}$, $\mu_e = 1.6 \text{ GPa}$, $\rho_e = 2500 \text{ kg/m}^3$, $Q_P = 30$, and $Q_S = 30$. All material parameters are given for the reference frequency $\omega_r = 120\pi \text{ Hz}$. Attenuation, see Appendix A, is modeled with $N = 3$ mechanisms in both water storage reservoir and the surrounding medium.

Table 1: Material parameter bounds assumed for the water storage reservoir.

variable name	symbol (unit)	Minimum value	Maximum value
Solid density	$\rho_s \text{ (kg/m}^3\text{)}$	2400	2800
Solid bulk modulus	$\kappa_s \text{ (GPa)}$	45	55
Frame bulk modulus	$\kappa_{fr} \text{ (GPa)}$	0.008	0.05
Frame shear modulus	$\mu_{fr} \text{ (GPa)}$	0.002	0.04
Tortuosity	τ	1.1	1.6
Porosity	$\phi \text{ (\%)}$	30	40
Quality factor	$Q_{\mu_{fr}}$	15	50
Quality factor	Q_{κ_s}	80	120
Quality factor	$Q_{\kappa_{fr}}$	15	50

The water content in the porous storage reservoir can be calculated by multiplying the volume of the water-saturated domain by the porosity. In the current work, the amount of water is calculated only from the water-saturated zone that is located exactly under the array or receivers.

2.2 Source function normalization

The observation model

$$V = A(\mathbf{m}) + e \quad (4)$$

$$= X + e, \quad (5)$$

consists of measurement data vector $V = [v_s, w_s]^\top$, forward model A , model parameters \mathbf{m} , and noise e . The noise model is assumed Gaussian, see Section 4 for more details.

For the applied inversion technique, the seismic source function needs to be known. In this paper, the effect from the source wavelet is marginalized via deconvolution operation.

We transform transient signals to the frequency domain and as a system response function, we assume data from the additional reference data point, shown in Fig. 1. Thus, the above observation model (5) is replaced by

$$\frac{F(V)}{F(V_{\text{ref}})} = \frac{F(X)}{F(X_{\text{ref}})} + \hat{e} \quad (6)$$

$$\hat{V} = \hat{X} + \hat{e}, \quad (7)$$

where F denotes the Fourier transform, subscript ref denotes the data on the reference point, and \hat{e} is the noise in the frequency domain formulation after the normalization. Equation (7) may become ill-conditioned when the denominator approaches zero. Thus, as in [33], the Wiener filtering is used to regularize the model. For the regularization coefficient, we use 0.001.

3 Discontinuous Galerkin method

As the physical model for the wave problems studied in this paper, we use a coupled poroviscoelastic-viscoelastic model. The governing equations, i.e. the Biot's poroviscoelastic wave equation and the viscoelastic wave equation, are given in Appendix A. For the applied numerical method, the coupled model is expressed as a first-order hyperbolic system [13].

In the current work, we operate in the Biot's low-frequency regime, see physical parameter choices in Section 2.1 and discussion in Section A.1, which leads to a stiff PDE system to solve. We apply the Godunov splitting [22] to handle the stiffness of the system. The Godunov splitting separates the dissipative component from the conservation term at each time step. As done, for example in [32], also here we solve the stiff part of the system analytically while the non-stiff part is solved numerically. More precisely, the spatial derivatives of the first-order hyperbolic system are approximated using the nodal discontinuous Galerkin (DG) method [17], while the time integration is carried out by the third-order Adams-Bashforth scheme [14].

In the discretized system, we use tetrahedral elements to discretize the model geometry into N_{el} elements. To obtain a strong form, in the DG formulation separately for each element, we multiply the hyperbolic system by a local test function and integrate by parts twice to obtain an elementwise variational formulation. As the numerical flux, i.e. the physical connection between adjacent elements, we use the upwind scheme [13]. For a more detailed discussion of the DG method, we refer to [17] and references therein.

3.1 Implementation

The current software is written in C/C++ programming language. The communication between different computational CPU nodes is handled using the message passing interface. Currently, the software uses constant order basis functions and hence the main reason for the different computational load on each element comes from the selected physical model (viscoelastic or poroviscoelastic). The computational load between different elements is balanced by the parMetis software in such a way that each element has an individual weight based on its physical model. Finally, the Open Concurrent Compute

Abstraction (OCCA) [26] library is used for communicating between CPU and GPU and also the computations on the graphics units. The CSC's Puhti environment [1] is used for calculations. All the computations shown in the following sections are done Puhti's NVIDIA Volta V100 graphics cards.

4 Neural networks

In this work, we use a fully connected neural network to recover the amount of stored water (i.e. one output value) from the synthetic seismic data. The simulated data V is down-sampled to a sampling frequency of 4 kHz and then contaminated by noise and then transformed to the frequency domain and deconvoluted with the reference data. Input data for neural network algorithm contains the stacked real and imaginary parts, i.e. $[\mathbb{R}(\hat{X}), \mathbb{I}(\hat{X})]^\top$ or $[\mathbb{R}(\hat{V}), \mathbb{I}(\hat{V})]^\top$. From the frequency spectrum, we select 12 frequencies varying from 35 Hz to 90 Hz, leading to a total input size of $33 \times 12 \times 2 \times 2 = 1584$.

An important part of a machine learning system are the choices for the network architecture. In this paper, the architecture is chosen as follows. The optimizer algorithm is set to be Adam [18]. We assume that the architecture contains either 1, 2, 3, or 4 hidden layers. For each layer choice, we run the KerasTuner [29] with Bayesian Optimization search algorithms to optimize the activation function, learning rate, and the number of neurons per hidden layer. As the possible activation function, we allow KerasTuner to choose 'relu', 'sigmoid', 'tanh', 'selu', 'swish', 'exponential', or 'LeakyReLU'. The number of neurons per layer is allowed to vary between [4, 1504], and as the learning rate, we let KerasTuner to choose [1e-3, 1e-4, 1e-5, 1e-6]. In addition to the previous steps, for each layer configuration, we run the KerasTuner for four values of batch size [32, 64, 128, 256]. The best performing network (mean absolute error with validation) is used as a selection criterion for the architecture.

After the hyperparameter tuning, the final architecture consists of 3 hidden layers with 1034 (layer 1), 594 (layer 2), and 184 (layer 3) neurons, swish activation function, learning rate 1e-4, and batch size 128. On the output layer, we use linear activation. The early stopping was also activated both in the hyperparameter tuning and actual training phases. We used the Python library TensorFlow [3] as a computing interface with Keras backend [10] for programming.

Training and validation databases and noise model

In the simulations described in the following, the length of the time step Δt for the applied Adams-Bashforth scheme is computed from

$$\Delta t = \min \left(\frac{0.4h^{(\ell)}}{c_{\max}^{(\ell)}(N_b + 1)^2} \right), \quad \ell = 1, \dots, N_{el}, \quad (8)$$

where $c_{\max}^{(\ell)}$ is the maximum wave speed on the element ℓ , N_b is the basis order, and $h^{(\ell)}$ is the (largest) inscribed sphere diameter of the element ℓ .

The initial step of (supervised) machine learning (ML) algorithm implementation is the creation of training and validation databases. The generation procedure of physical parameters is used to collect each sample in training, validation, and test data sets. The

acquisition geometry of the forward modeling on each sample is the same as described previously. We created 15000 training samples using computational grids with approximately 2 elements per shortest, inviscid material model-based, wavelength. For each element, the fifth-order polynomial basis function orders are used. An extra validation database of 3000 samples is also prepared to assess the models during the training phase to monitor the network’s generalization capabilities. Similarly, as with the training samples, we use fifth-order polynomials with the DG solver but the element size criteria is relaxed to approximately 1.9 elements per shortest wavelength. We use the Gaussian source function (1) for all training and validation samples.

All samples of the train and validation databases are contaminated with Gaussian noise. To be more specific, we make five copies of each sample in the database, and add noise for a sample as follows:

$$X_\ell^{\text{noised}} = X_\ell + A\alpha\epsilon^A + B|X_\ell|\epsilon^B, \quad (9)$$

where $\epsilon^A \sim \mathcal{N}(0, 1)$ and $\epsilon^B \sim \mathcal{N}(0, 1)$ are Gaussian random vectors and α is the largest absolute value of the training database. The second term represents additive (stationary) white noise. The coefficients A and B are randomized from the uniform distribution for each sample. To include a wide range of noise levels that are compatible with the amplitudes of the real noises the standard deviation of the white noise component varies uniformly between $[0.1 - 0.5]\%\alpha$ and the standard deviation of the relative component is between $[0 - 2]\%|X_\ell|$. The total number of samples in the training database is $5 \times 15000 = 75000$ and in the validation database $5 \times 3000 = 15000$.

5 Results

As a test dataset for the trained neural network, we use an additional 3000 samples. To ensure different numerical noise in the database, we use sixth-order basis orders for the DG solver in addition to 2.2 elements per shortest (inviscid-based) wavelength criterion for grid density. In addition, we assume a first derivative Gaussian function (2) as a source wavelet.

Snapshots of a noiseless total velocity field $\sqrt{u_s^2 + v_s^2 + w_s^2}$ from one sample in the test database are shown in Fig. 2. For the velocity field, u_s is the x -directional component of the solid velocity. For the visualized case, the water table level is at $z = -0.89$ m. The snapshots are shown at two time instants, 63.45 ms (left panel) and 131.72 ms (right panel). At the first time instant incident waves have reached the surface between air-saturated and surrounding elastic material at $x = 7.1$ m. We also observe the first reflection on the ground surface that originated from the bottom surface of the water storage. Snapshots on the right panel shows strong reflection from the surface between air-saturated zone and the surrounding elastic material. In addition, the effect from the water table level can be seen more clearly on the $x = 0$ cross section graph.

The test data comprise four different noise levels to study the network’s sensitivity to noise contamination. The same noise model (9), as used with the training and validation samples, is used also with test samples but the parameters A and B are fixed instead of randomized. Parameter choices are shown in Table 2. Combinations are selected in such a way that the first noise level corresponds to the very small noise amplitude, then the

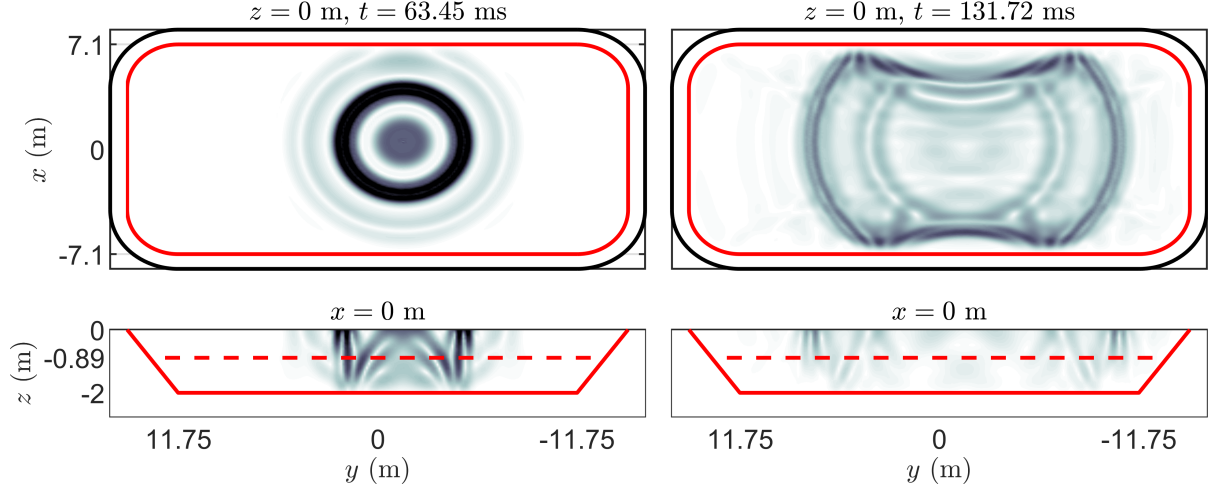


Figure 2: Snapshots of the total velocity field on two cross sections at two time instants. The zero coordinate axis and time instant are shown in the title. In the figures, the solid red line denotes the surface between the water storage reservoir and surrounding material and the dashed red line is the water table level ($z = -0.89$ m). On the top row, the solid black line shows the boundary for the exterior surface.

second combination leads to a moderate noise level, the third to a high noise amplitude, and the final fourth corresponds to an extreme noise level. The values of the fourth noise level exceed the values used for the training database.

Table 2: Noise amplitude parameters A and B for different noise levels (NL).

Noise parameter	NL ₁	NL ₂	NL ₃	NL ₄
A	0.001	0.0025	0.005	0.01
B	0.0	0.01	0.02	0.05

Figure 3 shows noisy seismograms for the same model as shown in Fig. 2. As for the noise level, we assume NL₃. Velocity components on the reference point are shown both with and without noise to illustrate the noise level. The bottom row shows the data in the frequency domain, separately real and imaginary parts of the velocity components.

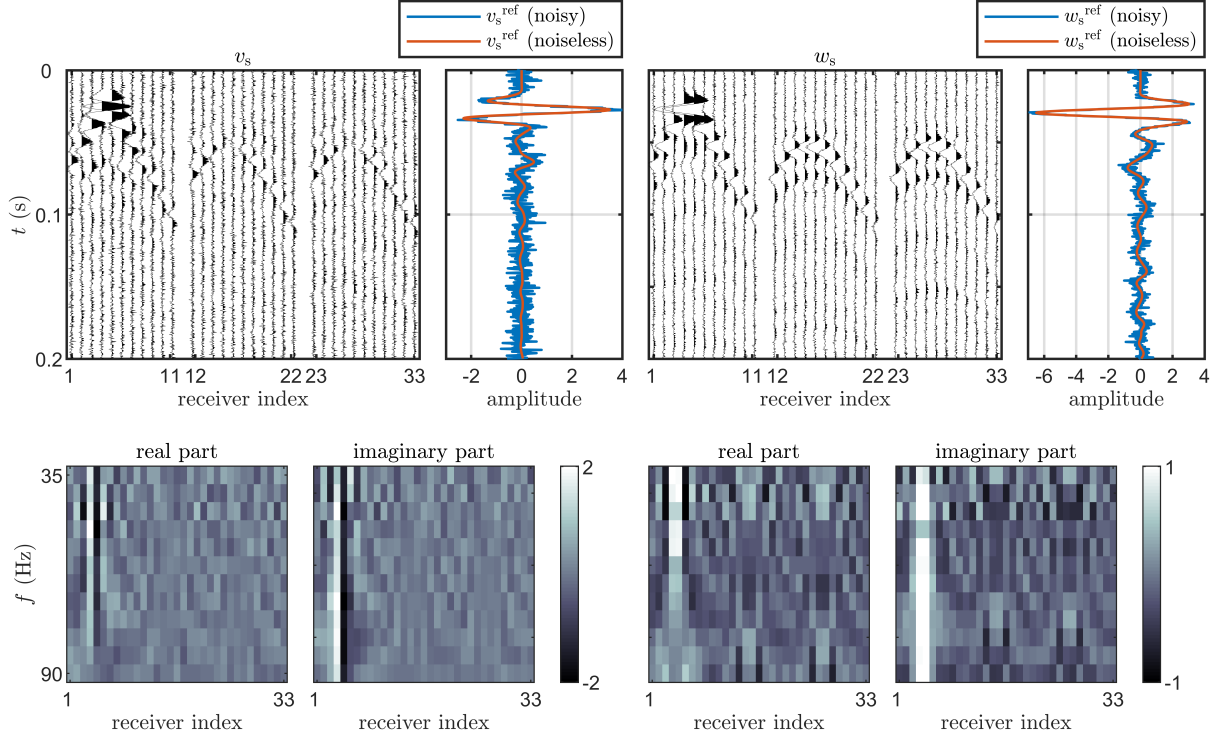


Figure 3: An example sample in the test database. Transient data is shown on the top row and frequency domain data on the bottom row. In addition, the left column shows the v_s component, and the right column the w_s component.

5.1 Predictions of water content

Figure 4 shows the true water content V_{true} (cubic meters) versus its predicted values V_{est} (cubic meters), each figure accompanied by a histogram of relative prediction errors V_{err} . The test dataset has four levels of noise numbered in Table 2 corresponding to the respective panels in Fig. 4. With increasing noise, the histograms slightly spread, which is concretely shown in Table 3 with the mean absolute error and root-mean-square error as criteria. Clearly this can be seen in the case of the extreme noise amplitude NL_4 , which goes beyond the values used in the training stage.

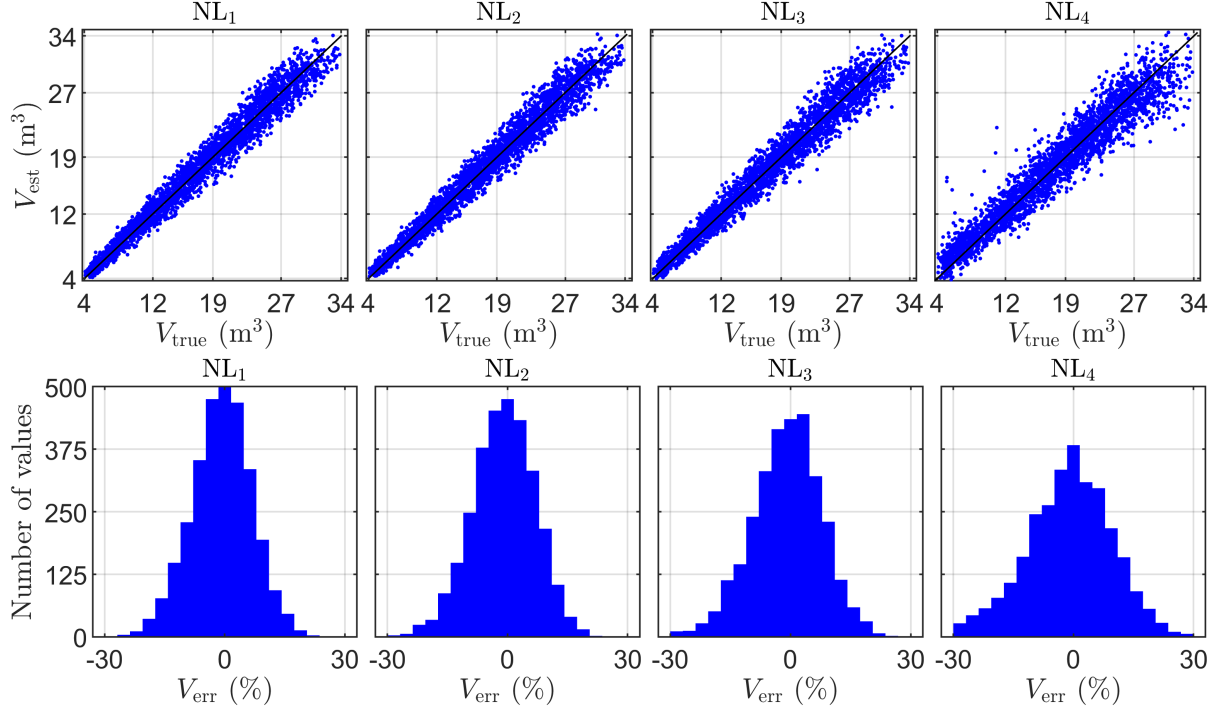


Figure 4: Estimated volumes of water as a function of true value and the relative error histogram for four noise level configurations. The noise level varies from low to extreme from left to right.

5.1.1 SHAP analysis

To investigate the contribution of individual data inputs, we use a feature contribution method called SHAP (SHapley Additive exPlanations) to explain the predictions. We use the Python library called Shap [23], and apply the DeepExplainer algorithm for 10000 randomly selected samples from the training database for building the explainer model. The model is then applied to a randomly selected set of 1000 samples from the test database (NL₂). The model gives the SHAP value for each unit of the input data (see Fig. 3 (bottom)), but here we are more interested to investigate the data contribution at the receiver level. Hence, we take the absolute value of each SHAP value and average receiver wise over the test samples as shown in Fig. 5. The result shows that the receivers 4, 5, 6, 3, 7, and 2 are the most contributing to predicting the model's output.

Next, we construct two new receiver configurations and train the neural network model for these. For the first configuration, we select six receivers having the largest SHAP values (see Fig. 5) and for the second configuration, we randomly select six receivers from the full sensor array. The network architecture consists of 3 hidden layers, learning rate 1e-4, swish activation function, and batch size 128, as used with the full receiver array. The number of neurons per hidden layer was optimized with KerasTuner. The network with SHAP analysis-based receiver selection consists of 1394 (layer 1), 894 (layer 2), and 564 (layer 3) neurons and with randomly selected receivers 1394 (layer 1), 1064 (layer 2), and 824 (layer 3) neurons. Note that we have used the same training database as with the full receiver array, just selecting the corresponding limited receiver array indices.

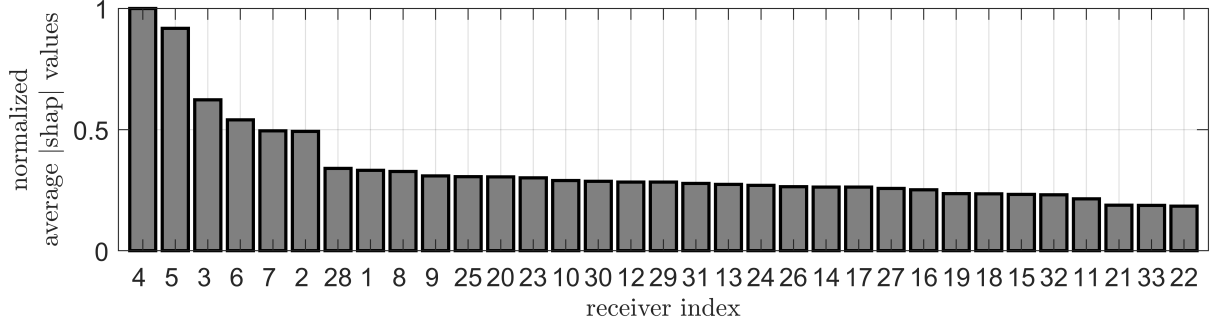


Figure 5: Average of the absolute SHAP values for each receiver. Values are sorted such that the most contributing receivers are on the left.

Figure 6 shows the estimated water content value as a function of the true water content value for both receiver configurations. Results indicate that the estimation accuracy is improved when using the SHAP analysis-based receivers. We also see that randomly selected receiver configuration leads to more outlier values.

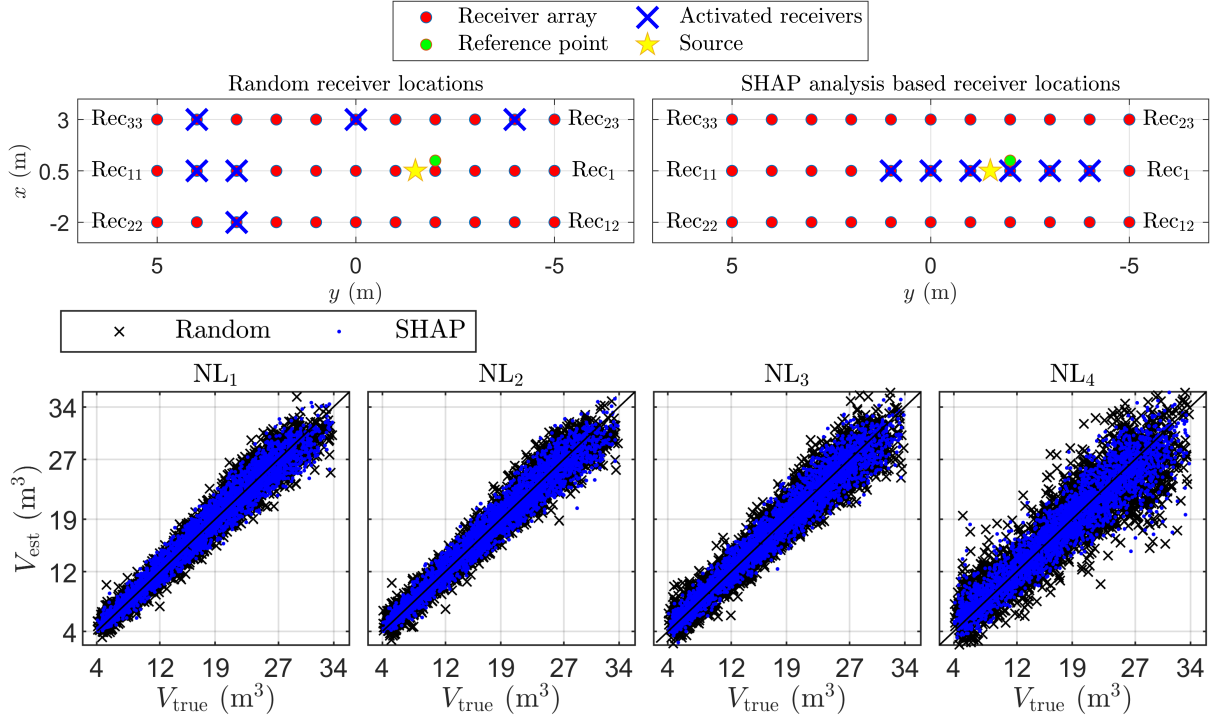


Figure 6: TopLeft: Randomly selected and TopRight: SHAP value-based 6 receivers. Estimated volumes of water as a function of the true value for four noise level configurations. In the bottom row, the noise level varies from low to extreme from left to right.

Table 3 lists the bias, mean absolute error, and root-mean-square error values for all three receiver configurations and the four noise levels. From the table, we see that the full receiver array leads to the most accurate results. On the other hand, we see that the SHAP analysis based and randomly selected six receivers lead to comparable numerical accuracy as the full receiver array. Finally, we see that the noise tolerance is slightly worse with randomly selected receivers.

Table 3: Bias, mean absolute error (MAE), and root-mean-square error (RMSE) for different noise levels were evaluated with the test database. The first four lines are for the full receiver array, the following four lines are for the most important SHAP-analysis based six receivers, and the last four lines the randomly selected six receivers.

Receiver array setup	Noise level	Bias (cubic meters)	MAE (cubic meters)	RMSE
full	NL ₁	-0.0760	0.9970	1.2915
	NL ₂	-0.0876	1.0312	1.3286
	NL ₃	-0.0525	1.1321	1.4605
	NL ₄	-0.0807	1.4958	1.9728
SHAP	NL ₁	-0.0290	1.1481	1.4933
	NL ₂	-0.0248	1.1980	1.5698
	NL ₃	-0.0421	1.3059	1.7087
	NL ₄	0.0373	1.7965	2.4338
random	NL ₁	-0.0776	1.1935	1.5382
	NL ₂	-0.0636	1.2542	1.6226
	NL ₃	0.0114	1.4780	1.9232
	NL ₄	0.0935	2.2569	3.0251

6 Conclusions

In this paper, the volume of water stored in a three-dimensional porous domain was estimated from synthetic seismic data. The study was purely numerical while the problem geometry is motivated by a real test site. As a physical model for wave propagation, we used a coupled poroviscoelastic–viscoelastic model, which was solved using the nodal discontinuous Galerkin method. The applied software simulates wave propagation in the time domain but in this study, the data were transformed to the frequency domain enabling us to normalize the effect from the source wavelet. The fully connected neural networks were used to recover the water content values from the frequency domain data.

The results of this study support the usage of a fully connected network for estimating the water storage reservoir parameters of interest with a wide selection of noise amplitudes while inconvenient parameters can profitably be marginalized. When compared to traditional full waveform inversion which would require the estimation of geometry and porosity, the suggested approach allowed water content estimates with a significant reduction in computational cost. One must note here, that the building of a training database for neural networks requires a lot of computational time and resources but once it is done and network trained, the estimates can be computed in real-time.

With the current problem setup, in principle, we could be able to estimate the water content accurately in the whole water-saturated subdomain but this cannot be generally assumed in the more realistic aquifer scenarios. This is related to the specific feature of the studied setup, where porous water storage is fully surrounded by a elastic domain, that strongly reflects waves back to porous domain.

We performed SHAP analysis on the developed machine learning model. The goal of the SHAP analysis was to investigate which of the receivers were the most contributing when estimating the volume of stored water. We also tested the effect of selecting much

fewer receivers than those used in the full receiver array. Here the selection was made based on the SHAP analysis and then randomly. It was evident that for the current problem setup, the characterization method together with the selection of the receivers is quite robust. We also want to emphasize that the SHAP analysis will most likely lead to totally different results when the problem geometry is more complex and also if the material fields are heterogeneous.

Future research could include a study with real data, its uncertainties, and also receiver-level SHAP analysis. It is possible that for the real data, we need to, for example, update the prior model for material and consider different network architectures, but these are topics of future research.

A Governing equations of the physical models

A.1 Biot's poroelastic wave equation with attenuation

In this paper, we use the Biot's wave equation [9]

$$\rho_a \frac{\partial^2 \mathbf{u}_s}{\partial t^2} + \rho_f \frac{\partial^2 \mathbf{w}}{\partial t^2} = \nabla \cdot \mathbf{T}, \quad (10)$$

$$\rho_f \frac{\partial^2 \mathbf{u}_s}{\partial t^2} + m \frac{\partial^2 \mathbf{w}}{\partial t^2} + \frac{\eta}{k} \frac{\partial \mathbf{w}}{\partial t} = \nabla \cdot \mathbf{T}_f, \quad (11)$$

to model wave propagation in three-dimensional poroelastic media. In model (10) and (11), \mathbf{u}_s is the solid displacement, \mathbf{u}_f the fluid displacement, and \mathbf{w} the relative displacement of fluid $\mathbf{w} = \phi(\mathbf{u}_f - \mathbf{u}_s)$, where ϕ is porosity. In addition, ρ_s is the solid density, ρ_f the fluid density, $\rho_a = (1 - \phi)\rho_s + \phi\rho_f$ is the average density, η is the viscosity and k is the permeability. In (11), $m = \rho_f\tau/\phi$, where τ is the tortuosity.

The lossless solid and fluid stress tensors \mathbf{T} and \mathbf{T}_f

$$\mathbf{T} = \begin{pmatrix} T_{11} & T_{12} & T_{13} \\ T_{12} & T_{22} & T_{23} \\ T_{13} & T_{23} & T_{33} \end{pmatrix}, \quad \mathbf{T}_f = \begin{pmatrix} -p_f & 0 & 0 \\ 0 & -p_f & 0 \\ 0 & 0 & -p_f \end{pmatrix}, \quad (12)$$

and can be expressed as

$$\mathbf{T} = 2\mu_{fr}\mathbf{E} + (\lambda \text{trace}(\mathbf{E}) - \alpha_B M \zeta) \mathbf{I}_3, \quad (13)$$

$$\mathbf{T}_f = (\alpha_B M \text{trace}(\mathbf{E}) - M \zeta) \mathbf{I}_3, \quad (14)$$

where μ_{fr} is the frame shear modulus, $\zeta = -\nabla \cdot \mathbf{w}$ is the variation of fluid content, and \mathbf{I}_3 denotes an identity matrix of size 3×3 . In addition, λ denotes a Lamé parameter and can be written as

$$\lambda = \kappa_{fr} + \alpha_B^2 M - \frac{2}{3}\mu_{fr}, \quad (15)$$

where κ_{fr} denote the frame bulk modulus. Let κ_s denote the solid bulk modulus, when we can write

$$\alpha_B = 1 - \frac{\kappa_{fr}}{\kappa_s} \quad (16)$$

and

$$M = \frac{\kappa_s}{\alpha_B - \phi(1 - \kappa_s/\kappa_f)}, \quad (17)$$

where κ_f is the fluid bulk modulus. In Eqs. (13) - (14), \mathbf{E} denote the solid strain tensor and can be written as

$$\mathbf{E} = \begin{pmatrix} \epsilon_{11} & \epsilon_{12} & \epsilon_{13} \\ \epsilon_{12} & \epsilon_{22} & \epsilon_{23} \\ \epsilon_{13} & \epsilon_{23} & \epsilon_{33} \end{pmatrix}, \quad (18)$$

where the ϵ_{ij} , $i, j = 1, 2, 3$ are components of the tensor. For a detailed derivation see [9].

As discussed in [9], viscoelasticity can be introduced into Biot's poroelastic equations for modelling attenuation mechanisms related to the kinetic energy (viscodynamic dissipation) and the potential energy (stiffness dissipation).

The viscodynamic dissipation effect can be further divided into the low- and high-frequency regimes. The main difference between these regimes is that for low frequencies the Pousselle assumption is valid and inertial forces are negligible to viscous forces. At higher frequencies, inertial forces are no longer negligible, and the viscous resistance to fluid flow given by the coefficient of the dissipative term is frequency-dependent. The Biot's characteristic frequency f_c can be used to distinguish between these frequency regimes:

$$f_c = \frac{\eta\phi}{2\pi\tau\rho_f k}, \quad (19)$$

where η is the fluid viscosity, ϕ porosity, τ tortuosity, ρ_f fluid density, and k permeability.

The stiffness dissipation and the applied model is discussed next in Section A.1.1.

A.1.1 Stiffness dissipation

In this work, the stiffness attenuation is modelled using the generalized Maxwell body (GMB) rheology. For a detailed discussion of the GMB, we refer to [27]. To include the stiffness dissipation in the poroelastic media, we follow [37] and re-write solid tensor \mathbf{T}

components as

$$T_{11} = (\lambda + 2\mu_{\text{fr}})^U \epsilon_{11} + \lambda^U \epsilon_{22} + \lambda^U \epsilon_{33} - (\alpha_{\text{B}} M)^U \zeta - \sum_{n=1}^N \left((\lambda + 2\mu_{\text{fr}})^U Y_{\lambda+2\mu_{\text{fr}}}^{(n)} \theta_{\epsilon_{11}}^{(n)} + \lambda^U Y_{\lambda}^{(n)} \theta_{\epsilon_{22}}^{(n)} + \lambda^U Y_{\lambda}^{(n)} \theta_{\epsilon_{33}}^{(n)} - (\alpha_{\text{B}} M)^U Y_{\alpha_{\text{B}} M}^{(n)} \theta_{\zeta}^{(n)} \right) \quad (20)$$

$$T_{22} = \lambda^U \epsilon_{11} + (\lambda + 2\mu_{\text{fr}})^U \epsilon_{22} + \lambda^U \epsilon_{33} - (\alpha_{\text{B}} M)^U \zeta - \sum_{n=1}^N \left(\lambda^U Y_{\lambda}^{(n)} \theta_{\epsilon_{11}}^{(n)} + (\lambda + 2\mu_{\text{fr}})^U Y_{\lambda+2\mu_{\text{fr}}}^{(n)} \theta_{\epsilon_{22}}^{(n)} + \lambda^U Y_{\lambda}^{(n)} \theta_{\epsilon_{33}}^{(n)} - (\alpha_{\text{B}} M)^U Y_{\alpha_{\text{B}} M}^{(n)} \theta_{\zeta}^{(n)} \right) \quad (21)$$

$$T_{33} = \lambda^U \epsilon_{11} + \lambda^U \epsilon_{22} + (\lambda + 2\mu_{\text{fr}})^U \epsilon_{33} - (\alpha_{\text{B}} M)^U \zeta - \sum_{n=1}^N \left(\lambda^U Y_{\lambda}^{(n)} \theta_{\epsilon_{11}}^{(n)} + \lambda^U Y_{\lambda}^{(n)} \theta_{\epsilon_{22}}^{(n)} + (\lambda + 2\mu_{\text{fr}})^U Y_{\lambda+2\mu_{\text{fr}}}^{(n)} \theta_{\epsilon_{33}}^{(n)} - (\alpha_{\text{B}} M)^U Y_{\alpha_{\text{B}} M}^{(n)} \theta_{\zeta}^{(n)} \right) \quad (22)$$

$$T_{12} = 2\mu_{\text{fr}}^U \epsilon_{12} - \sum_{n=1}^N 2\mu_{\text{fr}}^U Y_{\mu_{\text{fr}}}^{(n)} \theta_{\epsilon_{12}}^{(n)}, \quad (23)$$

$$T_{13} = 2\mu_{\text{fr}}^U \epsilon_{13} - \sum_{n=1}^N 2\mu_{\text{fr}}^U Y_{\mu_{\text{fr}}}^{(n)} \theta_{\epsilon_{13}}^{(n)}, \quad (24)$$

$$T_{23} = 2\mu_{\text{fr}}^U \epsilon_{23} - \sum_{n=1}^N 2\mu_{\text{fr}}^U Y_{\mu_{\text{fr}}}^{(n)} \theta_{\epsilon_{23}}^{(n)}, \quad (25)$$

and \mathbf{T}_{f} components as

$$-p_{\text{f}} = (\alpha_{\text{B}} M)^U \epsilon_{11} + (\alpha_{\text{B}} M)^U \epsilon_{22} + (\alpha_{\text{B}} M)^U \epsilon_{33} - M^U \zeta - \sum_{n=1}^N \left((\alpha_{\text{B}} M)^U Y_{\alpha_{\text{B}} M}^{(n)} \theta_{\epsilon_{11}}^{(n)} + (\alpha_{\text{B}} M)^U Y_{\alpha_{\text{B}} M}^{(n)} \theta_{\epsilon_{22}}^{(n)} + (\alpha_{\text{B}} M)^U Y_{\alpha_{\text{B}} M}^{(n)} \theta_{\epsilon_{33}}^{(n)} - M^U Y_M^{(n)} \theta_{\zeta}^{(n)} \right) \quad (26)$$

In (20)-(26) superscript U denotes un-relaxed material parameter. The formulas for getting un-relaxed material parameters will be given later in Section A.1.3.

The $7N$ memory variables $\boldsymbol{\theta}^{(n)} = (\theta_{\epsilon_{11}}^{(n)}, \theta_{\epsilon_{22}}^{(n)}, \theta_{\epsilon_{33}}^{(n)}, \theta_{\epsilon_{12}}^{(n)}, \theta_{\epsilon_{13}}^{(n)}, \theta_{\epsilon_{23}}^{(n)}, \theta_{\zeta}^{(n)})$ introduced in (20)-(26) satisfy the ordinary differential equations

$$\frac{\partial \theta_j^{(n)}}{\partial t} = \omega^{(n)} \left(\epsilon_j - \theta_j^{(n)} \right), \quad j = 1, \dots, 7, \quad (27)$$

where $\omega^{(n)}$ are the relaxation frequencies of the different mechanisms and $\boldsymbol{\epsilon} = (\epsilon_{11}, \epsilon_{22}, \epsilon_{33}, \epsilon_{12}, \epsilon_{13}, \epsilon_{23}, \zeta)$.

A.1.2 Q Transformation rule

In the stiffness dissipation model, we assume that the quality factors for the attenuation of the shear $Q_{\mu_{\text{fr}}}$ and bulk $Q_{\kappa_{\text{fr}}}$ moduli in the frame, solid-fluid coupling $Q_{\kappa_{\text{s}}}$, and bulk modulus of the saturated fluid $Q_{\kappa_{\text{f}}}$ are known. We denote $Q = (Q_{\mu_{\text{fr}}}, Q_{\kappa_{\text{s}}}, Q_{\kappa_{\text{fr}}}, Q_{\kappa_{\text{f}}})$ and follow the transformation rule steps given in [37].

The Kjartansson model [19] enables us to calculate the complex valued, frequency dependent, parameters $\bar{M}(\omega) = (\bar{M}_{\mu_{\text{fr}}}, \bar{M}_{\kappa_{\text{s}}}, \bar{M}_{\kappa_{\text{fr}}}, \bar{M}_{\kappa_{\text{f}}})$ and these can be written as

$$\bar{M}_j = M_j^R \cos^2 \left(\frac{\pi\gamma}{2} \right) \left(\frac{i\omega}{\omega_r} \right)^{2\gamma}, \quad j = 1, \dots, 4, \quad (28)$$

where $\gamma = \pi^{-1} \arctan(Q_j^{-1})$. In (28), the $M^R = (M_{\mu_{\text{fr}}^R}, M_{\kappa_s^R}, M_{\kappa_{\text{fr}}^R}, M_{\kappa_f^R})$ denotes a vector containing the material parameters obtained at a reference frequency ω_r . Next the complex valued parameters are substituted to (15), (16), and (17) to get the complex valued $(\bar{\lambda} + 2\bar{\mu}_{\text{fr}})^R$, $\bar{\alpha}_B^R$, and \bar{M}^R .

The frequency dependent quality factors $\hat{Q}(\omega) = (Q_{\lambda+2\mu_{\text{fr}}}, Q_{\mu_{\text{fr}}}, Q_{\alpha_B M}, Q_M)$

$$\hat{Q}_j(\omega) = \frac{\Re(\hat{M}_j)}{\Im(\hat{M}_j)}, \quad j = 1, \dots, 4, \quad (29)$$

where $\hat{M}(\omega) = (\hat{M}_{\lambda+2\mu_{\text{fr}}}, \hat{M}_{\mu_{\text{fr}}}, \hat{M}_{\alpha_B M}, \hat{M}_M)$. Finally, we apply a linear optimization procedure [15] to get anelastic coefficients

$$\mathbf{Y}^{(n)} = (Y_{\lambda+2\mu_{\text{fr}}}^{(n)}, Y_{\mu_{\text{fr}}}^{(n)}, Y_{\alpha_B M}^{(n)}, Y_M^{(n)}). \quad (30)$$

A.1.3 Un-relaxed material parameters

To get the corresponding un-relaxed values, we apply [27]

$$\Phi_j^U = \Phi_j^R \frac{\sqrt{D_1^2 + D_2^2} + D_1}{2(D_1^2 + D_2^2)}, \quad (31)$$

$$D_1 = 1 - \sum_{n=1}^N \mathbf{Y}_j^{(n)} \frac{\omega_n^2}{\omega_n^2 + \omega_r^2}, \quad (32)$$

$$D_2 = \sum_{n=1}^N \mathbf{Y}_j^{(n)} \frac{\omega_n \omega_r}{\omega_n^2 + \omega_r^2}, \quad (33)$$

where $j = 1, \dots, 4$ and

$$\Phi^{U/R} = ((\lambda + 2\mu_{\text{fr}})^{U/R}, \mu_{\text{fr}}^{U/R}, (\alpha_B M)^{U/R}, M^{U/R}). \quad (34)$$

Finally, the un-relaxed λ and the anelastic coefficients Y_λ are obtained from

$$\lambda^U = (\lambda + 2\mu_{\text{fr}})^U - 2\mu_{\text{fr}}^U, \quad (35)$$

$$Y_\lambda^{(n)} = \frac{(\lambda + 2\mu_{\text{fr}})^U Y_{\lambda+2\mu_{\text{fr}}}^{(n)} - 2\mu_{\text{fr}}^U Y_{\mu_{\text{fr}}}^{(n)}}{(\lambda + 2\mu_{\text{fr}})^U - 2\mu_{\text{fr}}^U}. \quad (36)$$

A.2 Viscoelastic wave equation

In this study, wave propagation also in a purely elastic medium is considered. Expressed as a second-order system, the elastic wave equation in three-dimensions takes the form [5]

$$\rho_e \frac{\partial^2 \mathbf{u}_e}{\partial t^2} = \nabla \cdot \mathbf{S}, \quad (37)$$

where \mathbf{u}_e is displacement, ρ_e is density, and \mathbf{S} is a stress tensor. For the studied case in this paper, \mathbf{S} may be written in the usual form

$$\mathbf{S} = 2\mu_e \mathbf{E} + \lambda_e \text{trace}(\mathbf{E}) \mathbf{I}_3, \quad (38)$$

where \mathbf{E} is the solid strain tensor and μ_e and λ_e are Lamé parameters.

To include attenuation of elastic waves, we approximate the material as a viscoelastic medium. We use the GMB rheological type [27] and, we re-write the solid tensor \mathbf{S} components as [36]

$$S_{11} = (\lambda_e + 2\mu_e)^U \epsilon_{11} + \lambda_e^U \epsilon_{22} + \lambda_e^U \epsilon_{33} - \sum_{n=1}^N \left((\lambda_e + 2\mu_e)^U Y_{\lambda_e + 2\mu_e}^{(n)} \theta_{\epsilon_{11}}^{(n)} + \lambda_e^U Y_{\lambda_e}^{(n)} \theta_{\epsilon_{22}}^{(n)} + \lambda_e^U Y_{\lambda_e}^{(n)} \theta_{\epsilon_{33}}^{(n)} \right), \quad (39)$$

$$S_{22} = \lambda_e^U \epsilon_{11} + (\lambda_e + 2\mu_e)^U \epsilon_{22} + \lambda_e^U \epsilon_{33} - \sum_{n=1}^N \left(\lambda_e^U Y_{\lambda_e}^{(n)} \theta_{\epsilon_{11}}^{(n)} + (\lambda_e + 2\mu_e)^U Y_{\lambda_e + 2\mu_e}^{(n)} \theta_{\epsilon_{22}}^{(n)} + \lambda_e^U Y_{\lambda_e}^{(n)} \theta_{\epsilon_{33}}^{(n)} \right), \quad (40)$$

$$S_{33} = \lambda_e^U \epsilon_{11} + \lambda_e^U \epsilon_{22} + (\lambda_e + 2\mu_e)^U \epsilon_{33} - \sum_{n=1}^N \left(\lambda_e^U Y_{\lambda_e}^{(n)} \theta_{\epsilon_{11}}^{(n)} + \lambda_e^U Y_{\lambda_e}^{(n)} \theta_{\epsilon_{22}}^{(n)} + (\lambda_e + 2\mu_e)^U Y_{\lambda_e + 2\mu_e}^{(n)} \theta_{\epsilon_{33}}^{(n)} \right), \quad (41)$$

$$S_{12} = 2\mu_e^U \epsilon_{12} - \sum_{n=1}^N 2\mu_e^U Y_{\mu_e}^{(n)} \theta_{\epsilon_{12}}^{(n)}, \quad (42)$$

$$S_{13} = 2\mu_e^U \epsilon_{13} - \sum_{n=1}^N 2\mu_e^U Y_{\mu_e}^{(n)} \theta_{\epsilon_{13}}^{(n)}, \quad (43)$$

$$S_{23} = 2\mu_e^U \epsilon_{23} - \sum_{n=1}^N 2\mu_e^U Y_{\mu_e}^{(n)} \theta_{\epsilon_{23}}^{(n)}. \quad (44)$$

Similarly, as in the poroviscoelastic case, also in (39)-(44) superscript U denotes un-relaxed material parameter. In addition, the $6N$ memory variables $\boldsymbol{\theta}_e^{(n)} = (\theta_{\epsilon_{11}}^{(n)}, \theta_{\epsilon_{22}}^{(n)}, \theta_{\epsilon_{33}}^{(n)}, \theta_{\epsilon_{12}}^{(n)}, \theta_{\epsilon_{13}}^{(n)}, \theta_{\epsilon_{23}}^{(n)})$ satisfy the ordinary differential equations

$$\frac{\partial \theta_{e,j}^{(n)}}{\partial t} = \omega^{(n)} \left(\epsilon_{e,j} - \theta_{e,j}^{(n)} \right), \quad j = 1, \dots, 6, \quad (45)$$

where $\boldsymbol{\epsilon}_e = (\epsilon_{11}, \epsilon_{22}, \epsilon_{33}, \epsilon_{12}, \epsilon_{13}, \epsilon_{23})$.

Let us assume that the quality factors (Q_P, Q_S) for the pressure and shear waves are known. Then, the optimization procedure [15] can be applied to get anelastic coefficients $Y_P^{(n)}$ and $Y_S^{(n)}$ for viscoelastic pressure and shear wave propagation [27]. On the other hand, the anelastic coefficients in terms of the Lamé parameters λ_e and μ_e are obtained by the transformation [27]

$$\lambda_e^U Y_{\lambda_e}^{(n)} + 2\mu_e^U Y_{\mu_e}^{(n)} = (\lambda_e + 2\mu_e)^U Y_P^{(n)}, \quad (46)$$

$$Y_{\mu_e}^{(n)} = Y_S^{(n)}. \quad (47)$$

Equations (31)-(33), given in Section A.1.3, can be used for calculating un-relaxed material parameters with (in this case $j = 1, 2$)

$$\Phi^{U/R} = \left((\lambda_e + 2\mu_e)^{U/R}, \mu_e^{U/R} \right). \quad (48)$$

Acknowledgements

This work has been supported by the Academy of Finland (the Finnish Center of Excellence of Inverse Modeling and Imaging) and and Academy of Finland project 321761. The authors wish also to acknowledge CSC – IT Center for Science, Finland, for generous computational resources.

References

- [1] CSC - IT Center for Science Ltd, Computing environment Puhti. <https://docs.csc.fi/computing/systems-puhti/>. Accessed: Oct. 27, 2022.
- [2] Global issues, water. <https://www.un.org/en/global-issues/water>. Accessed: 29 August 2020.
- [3] M. Abadi, A. Agarwal, P. Barham, E. Brevdo, Z. Chen, C. Citro, G. S. Corrado, A. Davis, J. Dean, M. Devin, S. Ghemawat, I. Goodfellow, A. Harp, G. Irving, M. Isard, Y. Jia, R. Jozefowicz, L. Kaiser, M. Kudlur, J. Levenberg, D. Mané, R. Monga, S. Moore, D. Murray, C. Olah, M. Schuster, J. Shlens, B. Steiner, I. Sutskever, K. Talwar, P. Tucker, V. Vanhoucke, V. Vasudevan, F. Viégas, O. Vinyals, P. Warden, M. Wattenberg, M. Wicke, Y. Yu, and X. Zheng. TensorFlow: Large-scale machine learning on heterogeneous systems, 2015. Software available from tensorflow.org.
- [4] S. Adedibu and C. Abimbola. Insight into seismic refraction and electrical resistivity tomography techniques in subsurface investigations. *The Mining-Geology-Petroleum Engineering Bulletin*, 34(1):93–111, 2019.
- [5] K. Aki and P. G. Richards. *Quantitative Seismology*. University Science Books, 2002.
- [6] M. Araya-Polo, A. Adler, S. Farris, and J. Jennings. *Fast and Accurate Seismic Tomography via Deep Learning*, pages 129–156. Springer International Publishing, 2020.
- [7] M. Baharuddin, Z. Hazreek, M. Azman, and A. Madun. Prediction of groundwater level at slope areas using electrical resistivity method. In *Journal of Physics: Conference Series*, volume 995, page 012084. IOP Publishing, 2018.
- [8] J. Bear. *Dynamics of Fluids in Porous Media*. Courier Corporation, 1988.
- [9] J. Carcione. *Wave Fields in Real Media: Wave propagation in anisotropic, anelastic and porous media*. Elsevier, 2015.
- [10] F. Chollet et al. Keras. <https://keras.io>, 2015.
- [11] T. Clements and M. A. Denolle. Tracking groundwater levels using the ambient seismic field. *Geophysical Research Letters*, 45(13):6459–6465, 2018.
- [12] J. de la Puente. *Seismic wave simulation for complex rheologies on unstructured meshes*. PhD thesis, Ludwig-Maximilians-Universität, 2008.

- [13] N. F. Dudley Ward, S. Eveson, and T. Lähivaara. A discontinuous Galerkin method for three-dimensional poroelastic wave propagation: Forward and adjoint problems. *Computational Methods and Function Theory*, 21:737–777, 2021.
- [14] D. R. Durran. The third-order Adams-Bashforth method: An attractive alternative to leapfrog time differencing. *Monthly Weather Review*, 119:702–720, 1991.
- [15] H. Emmerich and M. Korn. Incorporation of attenuation into time-domain computations of seismic wave fields. *Geophysics*, 52(9):1252–1264, 09 1987.
- [16] Y. Guo, J. Huang, C. Cui, Z. Li, L. Fu, and Q. Li. Multi-source multi-scale source-independent full waveform inversion. *Journal of Geophysics and Engineering*, 16(3):479–492, 2019.
- [17] J. S. Hesthaven and T. Warburton. *Nodal Discontinuous Galerkin Methods: Algorithms, Analysis, and Applications*. Springer, 2007.
- [18] D. P. Kingma and J. Ba. Adam: A method for stochastic optimization, 2014.
- [19] E. Kjartansson. Constant Q-wave propagation and attenuation. *Journal of Geophysical Research: Solid Earth*, 84(B9):4737–4748, 1979.
- [20] T. Lähivaara, A. Malehmir, A. Pasanen, L. Kärkkäinen, J. M. Huttunen, and J. S. Hesthaven. Estimation of groundwater storage from seismic data using deep learning. *Geophysical Prospecting*, 67(8):2115–2126, 2019.
- [21] K. H. Lee and H. J. Kim. Source-independent full-waveform inversion of seismic data. *Geophysics*, 68(6):2010–2015, 2003.
- [22] R. Leveque. *Finite Volume Methods for Hyperbolic Problems*. Cambridge University Press, 2002.
- [23] S. M. Lundberg and S.-I. Lee. A unified approach to interpreting model predictions. *Advances in neural information processing systems*, 30, 2017.
- [24] S. Mao, A. Lecointre, R. D. van der Hilst, and M. Campillo. Space-time monitoring of groundwater fluctuations with passive seismic interferometry. *Nature Communications*, 13(1):1–9, 2022.
- [25] A. McClymont, M. Hayashi, L. Bentley, and J. Liard. Locating and characterising groundwater storage areas within an alpine watershed using time-lapse gravity, gpr and seismic refraction methods. *Hydrological Processes*, 26(12):1792–1804, 2012.
- [26] D. S. Medina, A. St-Cyr, and T. Warburton. OCCA: A unified approach to multi-threading languages. *arXiv preprint arXiv:1403.0968*, 2014.
- [27] P. Moczo, J. Kristek, and M. Gális. *The finite-difference modelling of earthquake motions: Waves and ruptures*. Cambridge University Press, 2014.
- [28] S. M. Mousavi and G. C. Beroza. Deep-learning seismology. *Science*, 377(6607):eabm4470, 2022.

- [29] T. O'Malley, E. Bursztein, J. Long, F. Chollet, H. Jin, L. Invernizzi, et al. Keras-tuner. <https://github.com/keras-team/keras-tuner>, 2019.
- [30] T. Perol, M. Gharbi, and M. Denolle. Convolutional neural network for earthquake detection and location. *Science Advances*, 4(2):e1700578, 2018.
- [31] J. E. Prentice. *Geology of construction materials*, volume 4. Springer Science & Business Media, 1990.
- [32] K. Shukla, J. S. Hesthaven, J. M. Carcione, R. Ye, J. de la Puente, and P. Jaiswal. A nodal discontinuous Galerkin finite element method for the poroelastic wave equation. *Computational Geosciences*, 23(3):595–615, 2019.
- [33] W. Wen and E. Kalkan. System identification based on deconvolution and cross correlation: An application to a 20-story instrumented building in Anchorage, Alaska. *Bulletin of the Seismological Society of America*, 107(2):718–740, 2017.
- [34] L. C. Wilcox, G. Stadler, C. Burstedde, and O. Ghattas. A high-order discontinuous Galerkin method for wave propagation through coupled elastic-acoustic media. *Journal of Computational Physics*, 229(24):9373–9396, 2010.
- [35] J. Xie, M. Yvonne Ou, and L. Xu. A discontinuous Galerkin method for wave propagation in orthotropic poroelastic media with memory terms. *Journal of Computational Physics*, 397:108865, 2019.
- [36] Q. Zhan, M. Zhuang, Q. Sun, Q. Ren, Y. Ren, Y. Mao, and Q. H. Liu. Efficient ordinary differential equation-based discontinuous galerkin method for viscoelastic wave modeling. *IEEE Transactions on Geoscience and Remote Sensing*, 55(10):5577–5584, 2017.
- [37] Q. Zhan, M. Zhuang, Z. Zhou, J.-G. Liu, and Q. H. Liu. Complete-Q model for poro-viscoelastic media in subsurface sensing: Large-scale simulation with an adaptive DG algorithm. *IEEE Transactions on Geoscience and Remote Sensing*, 57(7):4591–4599, 2019.